

27 1. Introduction

28 A seismic low-velocity zone (LVZ; Figure 1) between $\sim 100 - 250$ km depth is a prominent
 29 feature below the oceanic lithosphere that is consistently reported by global and local
 30 seismological models (e.g., Dalton et al., 2009). Since the LVZ was discovered by Gutenberg
 31 (1959), researchers have noted its overlap with the asthenosphere (Figure 1), the low-viscosity
 32 zone that facilitates mantle deformation beneath the tectonic plates (e.g., Richards et al., 2001).
 33 Indeed, the deformation of asthenospheric rocks is illuminated by a seismically-anisotropic
 34 layer (high anisotropy zone, Figure 1; e.g., Nettles and Dziewonski, 2008) that is produced by
 35 shear deformation of olivine (e.g., Tommasi et al., 1999; Jung and Karato, 2001). This
 36 deformation drives grain-size reduction (e.g., Behn et al., 2009), which can decrease both the
 37 seismic velocity (e.g., Faul and Jackson, 2005) and the effective mantle viscosity (e.g., Warren
 38 and Hirth, 2006; Hirth and Kohlstedt, 2003), potentially amplifying the deformation. Stiff plates
 39 may also trap partial melt (e.g., Chantel et al., 2016; Selway and O'Donnell, 2019; Debayle et
 40 al. 2020), reducing seismic velocities.

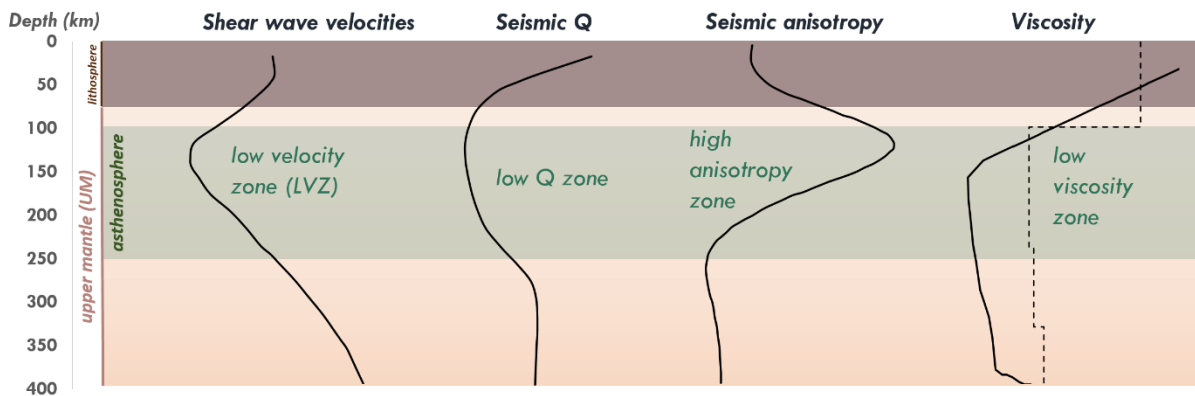


Figure 1. Schematic representation of seismic observations and inferred viscosities in the oceanic upper mantle (above 400 km) where low velocity, low Q, high radial anisotropy, and low viscosity zones exist within the same approximate depth range (the asthenosphere, green region). The shear wave velocity model shown is from Nettles and Dziewonski (2008) for 25-100 Myr oceanic plate ages, the global seismic Q factor is from Karaoglu and Romanowicz (2018), and the global seismic radial anisotropy is from Nettles and Dziewonski (2008) for mid-age oceans. The viscosity profiles are inferred from mantle flow models where the solid line is for purely temperature-dependent viscosity (Becker, 2006), and the dashed line is geoid-constrained viscosity (Steinberger and Calderwood, 2006).

41 In addition to reducing seismic wave speeds, both grain-size reduction and partial melt dissipate
42 seismic energy, and indeed the LVZ is approximately coincident with a zone of high seismic
43 attenuation (low seismic Q zone, Figure 1). The LVZ, the low-Q zone, and low viscosity
44 asthenosphere all overlap (Figure 1), and the coincident layer of seismic anisotropy suggests
45 that all three are linked together with asthenospheric deformation. Grain-size reduction, which
46 is driven by rock deformation, is an obvious explanation, because it reduces seismic velocity,
47 seismic Q, and effective viscosity. Indeed, without grain-size variations produced by
48 asthenospheric deformation, the forward-prediction of seismic structures (Figure S1) does not
49 reproduce the low Q zone in the asthenosphere, and the amplitude of the LVZ is underpredicted.
50 The patterns of rock deformation in the asthenosphere exert an important control on upper
51 mantle seismic properties, and indeed we can use seismic observations of the LVZ and low-Q
52 zone to constrain models of asthenospheric deformation.

53 Using grain size evolution models (e.g., Austin and Evans, 2007; Hall and Parmentier, 2003),
54 we investigate time-dependent depth variations of grain size resulting from flow-induced
55 deformation within the upper mantle. Behn et al. (2009) already showed the importance of grain
56 size evolution for the seismic structures associated with asthenospheric shear (Couette flow,
57 Figure 2a), but recent studies have suggested that pressure-driven (Poiseuille, Figure 2b) flow
58 may be the dominant mode of deformation within much of the upper mantle (e.g., Höink and
59 Lenardic, 2010; Semple and Lenardic, 2018). Couette flow arises due to the motion of a surface
60 plate that shears the asthenosphere below it in a linear fashion, while Poiseuille flow is induced
61 by pressure gradients across the upper mantle associated with mantle upwellings and
62 downwellings and/or lateral density variations. By developing an analytical model that
63 incorporates realistic upper mantle flow configurations (combined Couette and Poiseuille
64 flows), we determine how grain-size variations depend on flow drivers such as plate speed and
65 horizontal pressure gradient, and on mantle parameters such as water content and melt fraction.

66 Although water content (e.g., Karato and Jung, 1998; Karato 2012) does not significantly affect
67 seismic attenuation (Cline et al. 2018), it does affect viscosity (e.g., Mei and Kohlstedt, 2000;
68 Hirth and Kohlstedt, 2003). We also investigate feedbacks between grain-size, asthenosphere
69 flow, rheology, and deformation mechanism. From the modelled flow in the upper mantle, we
70 make predictions of seismic structures that can be tested against observations of seismic
71 velocity and attenuation in the upper mantle. This comparison places constraints on mantle
72 conditions and dominant flow types necessary to explain the observed LVZ and low Q zone.

73 **2. Types of flow in the oceanic upper mantle**

74 Several analytical and numerical studies show that flow in the upper mantle results from a
75 combination of Couette (plate-driven, Figure 2a) and Poiseuille (pressure-driven, Figure 2b)
76 flows (e.g., Lenardic et al., 2006; Höink and Lenardic, 2010; Natarov and Conrad, 2012). If
77 Couette flow occurs via dislocation creep, this shearing flow produces a lattice-preferred
78 orientation of olivine crystals that form a single seismically anisotropic layer (Figure 2a). Two
79 distinct anisotropic layers, as detected by Lin et al. (2016) at the top and the base of the
80 asthenosphere, can be formed by separate shear zones if the asthenosphere additionally hosts
81 Poiseuille flow (Figure 2b). If the upper mantle has a Newtonian rheology, a Newtonian
82 Poiseuille flow (termed $PFn1$ here, where ‘ $n1$ ’ denotes the stress exponent $n=1$, Figure 2b.1)
83 is produced. For a power-law rheology, the flow is dominated by the so-called “plug flow”
84 (termed $PFn3$ here, for $n=3$, Figure 2b.2), with approximately uniform velocity in the middle
85 of the low-viscosity layer, bounded above and below by zones of intense shear deformation
86 (Semple and Lenardic, 2018).

87 **3. Analytical plate- and pressure-driven flow model for the oceanic upper mantle**

88 We develop an analytical 1-D channel flow model (Sections 3.1 and 3.2) for the oceanic mantle
89 to investigate the effect of flow configurations on rheology (Section 4) and seismic structures

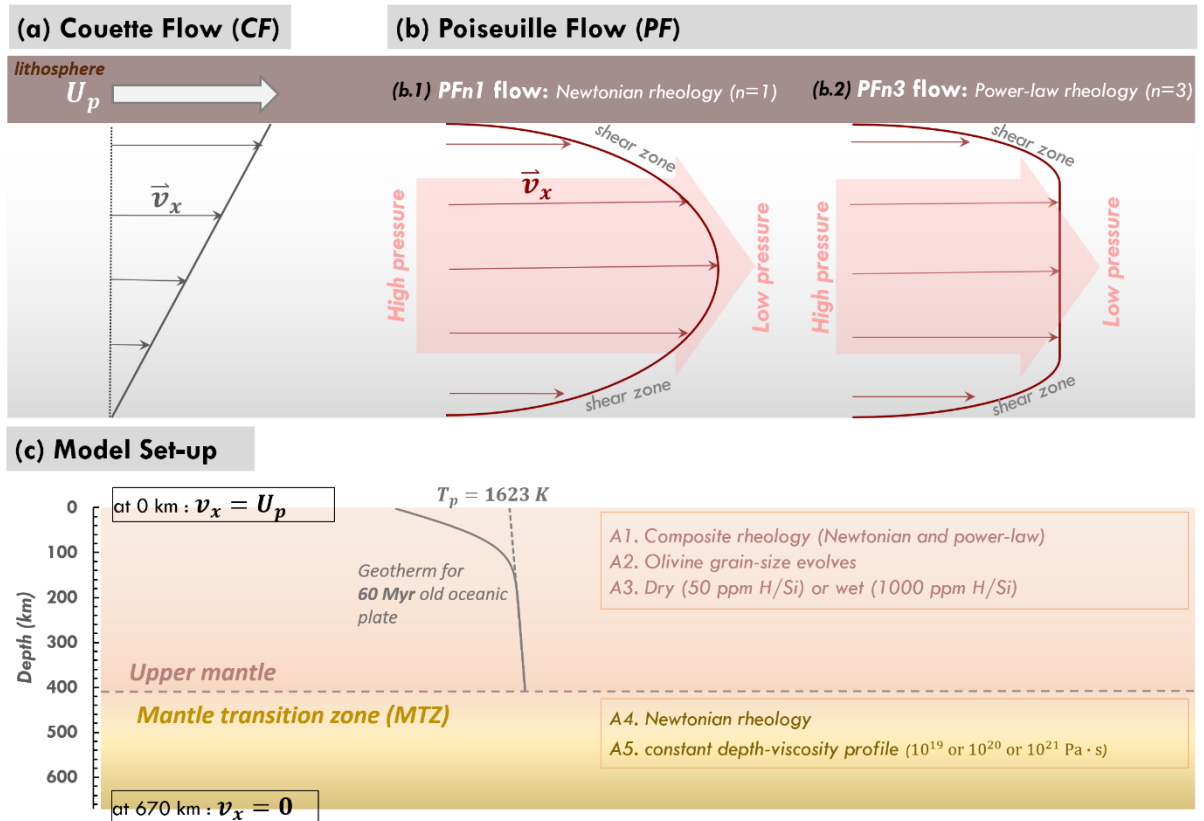


Figure 2. (a-b) Dominant flow regimes in the upper mantle: Sketch of flow velocities (\vec{v}_x) due to (a) Couette flow (CF) driven by surface plate motion and (b) Poiseuille flow (PF) driven by a lateral pressure gradient. The rheology of the upper mantle determines the PF flow configuration, where (b.1) a parabolic-shaped velocity profile arises if the rheology is Newtonian (termed PFn1 here), or (b.2) a plug flow arises for power-law rheology (termed PFn3 here). **(c) Model set-up.** We consider a 60 Myr old oceanic plate with 1623 K potential temperature (T_p) that results in a temperature profile shown in (c). We assume that the oceanic upper mantle (defined here as the region above 410 km) is governed by a composite olivine rheology, which is controlled by the geotherm, grain sizes and water content (dry or wet). We also consider the mantle transition zone (MTZ, 410 – 670 km) in our analytical model to investigate its effect on the flow configurations of the upper mantle flow region above it. Since the rheology of the MTZ is not well constrained by experiments, we assumed that it has a Newtonian rheology and a constant viscosity. With the calculated (above 410 km) and assigned (for the MTZ) rheologies, the flow velocities are calculated using Eqs. (6.2) and (A.5), where the boundary conditions are shown in (c).

90 (Section 5), particularly in the seismically anomalous and weak asthenosphere. We let the
 91 rheology of the mantle determine the style of flow and the associated flow rates and stresses
 92 (Section 3.2). At the same time, the flow alters the olivine grain size with time until the size
 93 stabilizes (Section 3.3) by utilizing the available grain size evolution models (e.g., Austin and
 94 Evans, 2007; Hall and Parmentier, 2003). Thus, the temporal evolution of olivine grain size
 95 requires us to also calculate the time-evolution of the shear stresses, horizontal velocities and

96 viscosities (Section 3.4). From this, we can account for possible feedbacks between flow
97 configurations, rheology, deformation, and grain-size.

98 **3.1 Model Set-up**

99 Since we do not know the appropriate depth and the velocity boundary condition at the base of
100 the asthenosphere (green region, Figure 1), we incorporate the entire oceanic mantle down to
101 670 km (including lithosphere, asthenosphere, upper mantle, and mantle transition zone; Figure
102 2c) into our model. We impose a plate speed U_p at 0 km to drive Couette flow (Figure 2a), and
103 a zero flow condition ($v_x = 0$) at 670 km, which assumes that flow is much slower in the highly
104 viscous lower mantle. We assign a lateral pressure gradient (dp/dx) across the layers above
105 670 km to drive Poiseuille flow (Figure 2b). From the U_p and dp/dx drivers, the resulting flow
106 configuration and the associated flow velocities (v_x) are determined by the composite rheology
107 above 410 km, and the assigned Newtonian rheology of the mantle transition zone (Section
108 3.2). The rheology above 410 km is dictated by the assigned water content (50 ppm H/Si or
109 1000 ppm H/Si) and melt fraction, the computed geotherm for a 60 Myr oceanic plate with 1623
110 K potential temperature (Figure 2c; using Equation (4.113) of Turcotte and Schubert (2014)),
111 and the deformation-dependent olivine grain size. This results in a cold and highly viscous
112 lithosphere at depths shallower than ~ 100 km and a deformable upper mantle layer between the
113 lithosphere and the mantle transition zone. Although the mantle transition zone (410 – 670 km)
114 may deform under dislocation creep (e.g., Ritterbex et al., 2020), we assigned a Newtonian
115 viscosity in the range $10^{19} - 10^{21}$ Pa·s (e.g., Kaufmann and Lambeck, 2000; Forte and
116 Mitrovica, 1996) because the flow laws for ringwoodite and wadsleyite (polymorphs of olivine
117 that are stable in the mantle transition zone) are not well constrained by experiments.

118 **3.2 Working equations for the 1D flow model**

119 Both plate- and pressure-driven flows are governed by the Navier-Stokes equation.

120
$$\rho \frac{D\vec{V}}{Dt} = -\nabla p + \vec{F} + \eta \nabla^2 \vec{V} \quad (1)$$

121 When neglecting the inertial term $\frac{D\vec{V}}{Dt}$ and body forces \vec{F} , we are left with pressure and viscous
 122 terms for a 1D model,

123
$$-\frac{\partial p}{\partial x} + \frac{\partial}{\partial z} \left(\eta(z) \frac{\partial v_x}{\partial z} \right) = 0 \quad (2.1)$$

124
$$-\frac{\partial p}{\partial x} + \frac{\partial}{\partial z} (\tau_{xz}) = 0 \quad (2.2)$$

125 where $\frac{\partial p}{\partial x}$ is a constant horizontal pressure gradient, $\eta(z)$ is depth-dependent viscosity, τ_{xz} is
 126 the shear stress, and v_x is the horizontal velocity (either plate-driven or pressure-driven).
 127 Integrating Equation (2.2) with respect to z yields an estimate of the shear stress $\tau_{xz} = \tau$
 128 induced by the flow at every layer i of our 1D model as described by

129
$$\tau_i = \frac{\partial p}{\partial x} z_i + C_i \quad (3)$$

130 where C_i is a constant of integration.

131 When assuming a composite rheology (that is, rheology controlled by both diffusion and
 132 dislocation creep), the total strain rate (Hirth and Kohlstedt, 1996) per layer is

133
$$\dot{\epsilon}_{total,i} = \dot{\epsilon}_{diff,i} + \dot{\epsilon}_{disl,i} = \frac{\sigma}{\eta_{eff,i}} \quad (4)$$

134 where $\dot{\epsilon}_{diff}$ is the strain rate for diffusion creep, $\dot{\epsilon}_{disl}$ is the strain rate for dislocation creep,
 135 η_{eff} is the effective viscosity, and σ is the differential stress which is equivalent to 2τ . We
 136 assume that $PFn1$ dominates for the diffusion creep regime ($n=1$) as predicted by Höink et al.
 137 (2011) and $PFn3$ dominates for dislocation creep regime ($n=3$) as illustrated by Semple and
 138 Lenardic (2018).

139 The strain-rate components are defined according to their relevant rheological relationships,

$$140 \quad \dot{\epsilon}_{diff,i} = A_{PFn1,i} \tau_i = \frac{\partial v_{PFn1,i}}{\partial z} \quad (5.1)$$

$$141 \quad \dot{\epsilon}_{disl,i} = A_{PFn3,i} \tau_i^3 = \frac{\partial v_{PFn3,i}}{\partial z} \quad (5.2)$$

$$142 \quad A_{PFn1,i} = A_{diff} C_{OH}^{r_{diff}} d^{-p_{diff}} \exp(\alpha_{diff} \varphi) \exp\left[-\frac{E_{diff} + PV_{diff}}{RT}\right] \quad (5.3)$$

$$143 \quad A_{PFn3,i} = A_{disl} C_{OH}^{r_{disl}} d^{-p_{disl}} \exp(\alpha_{disl} \varphi) \exp\left[-\frac{E_{disl} + PV_{disl}}{RT}\right] \quad (5.4)$$

144 by applying the empirically determined flow laws (Hirth and Kohlstedt, 2003). The $v_{PFn1,i}$ and
 145 $v_{PFn3,i}$ in Equations (5.1) and (5.2) are the horizontal velocities for *PFn1* and *PFn3* flow
 146 configurations, respectively. The parameters for the upper mantle defined in Equations (5.3)
 147 and (5.4) prescribe the rheological impact of grain-size d , water content C_{OH} , and melt fraction
 148 φ (other parameters are defined in Table S1; Supplementary Information). For the mantle
 149 transition zone with an assigned Newtonian rheology ($\dot{\epsilon}_{total} = \dot{\epsilon}_{diff}$ and $\eta_{eff} = \eta_{MTZ}$ where
 150 η_{MTZ} is the assigned viscosity), the parameters are $A_{PFn1,i} = 2/\eta_{MTZ}$ derived by combining
 151 Equations (5.1) and (4), and $A_{PFn3,i} = 0$.

152 The overall $v_{x,i}$ is $v_{PFn1,i} + v_{PFn3,i}$, where the velocity components are integrals of Equations
 153 (5.1) and (5.2) with respect to z , respectively:

$$154 \quad v_{x,i} = \int A_{PFn1,i} \tau_i dz + \int A_{PFn3,i} \tau_i^3 dz \quad (6.1)$$

155 Substituting the τ_i in Equation (6.1) with Equation (3), and then integrating them with respect
 156 to z yields:

$$157 \quad v_{x,i} = A_{PFn1,i} \left[\frac{1}{2} \frac{\partial p}{\partial x} z_i^2 + C_i z_i \right] + A_{PFn3,i} \left[\frac{1}{4} \left(\frac{\partial p}{\partial x} \right)^3 z_i^4 + C_i \left(\frac{\partial p}{\partial x} \right)^2 z_i^3 \right. \\ \left. + \frac{3}{2} C_i^2 \frac{\partial p}{\partial x} z_i^2 + C_i^3 z_i \right] + k_i \quad (6.2)$$

158 where k_i is the constant of integration and the involved parameters are summarized in Table S1
 159 (Supplementary Information). When $\frac{\partial p}{\partial x} = 0$, Equations (3) and (6.2) describe a Couette flow
 160 configuration.

161 Implementing the necessary boundary conditions and linearizing the problem as described in
 162 Supplementary Information B, we estimate the horizontal velocity (Equation 6.2) and shear
 163 stress (Equation 3) structures.

164 **3.3 Olivine grain size evolution model for the upper mantle**

165 During deformation, mineral grains in mantle rocks temporally evolve to a stable size for which
 166 the grain growth rate equilibrates with the grain reduction rate. We mainly employ the grain-
 167 size evolution model of Austin and Evans (2007),

$$168 \quad \text{AE07 model: } \dot{d} = p_g^{-1} d^{1-p_g} G_o \exp\left(-\frac{E_g + PV_g}{RT}\right) - \chi c^{-1} \gamma^{-1} \sigma \dot{\epsilon}_{disl} d^2 \quad (7)$$

169 where the first term describes the grain growth rate \dot{d}_{gg} , and the second term describes dynamic
 170 recrystallization rate \dot{d}_{dr} that results in grain size reduction. The parameter values used in this
 171 study are summarized in Table S1 (Supplementary Information). When there is no mechanical
 172 work or deformation (i.e., $\dot{\epsilon}_{disl} = 0$), the total grain size evolution is equivalent to the grain
 173 growth rate (first term, Equation 7). When deformation does occur, new grain boundaries may
 174 be created (second term > 0), which results in grain size reduction. Because larger grains are
 175 subdivided faster than smaller grains, the rate of grain size reduction (second term, Equation 7)
 176 increases with grain size. At depths with minimum stress, water promotes grain growth through
 177 significant reduction in $\dot{\epsilon}_{disl}$ (first term $>$ second term, Equation 7).

178 **3.4 Temporal evolution of olivine grain-size, rheology and flow configuration**

179 Using the detailed set-up described above and in Supplementary Information B, C and D, we
 180 investigate how the flow configuration, shear stress, rheology, and deformation evolve with

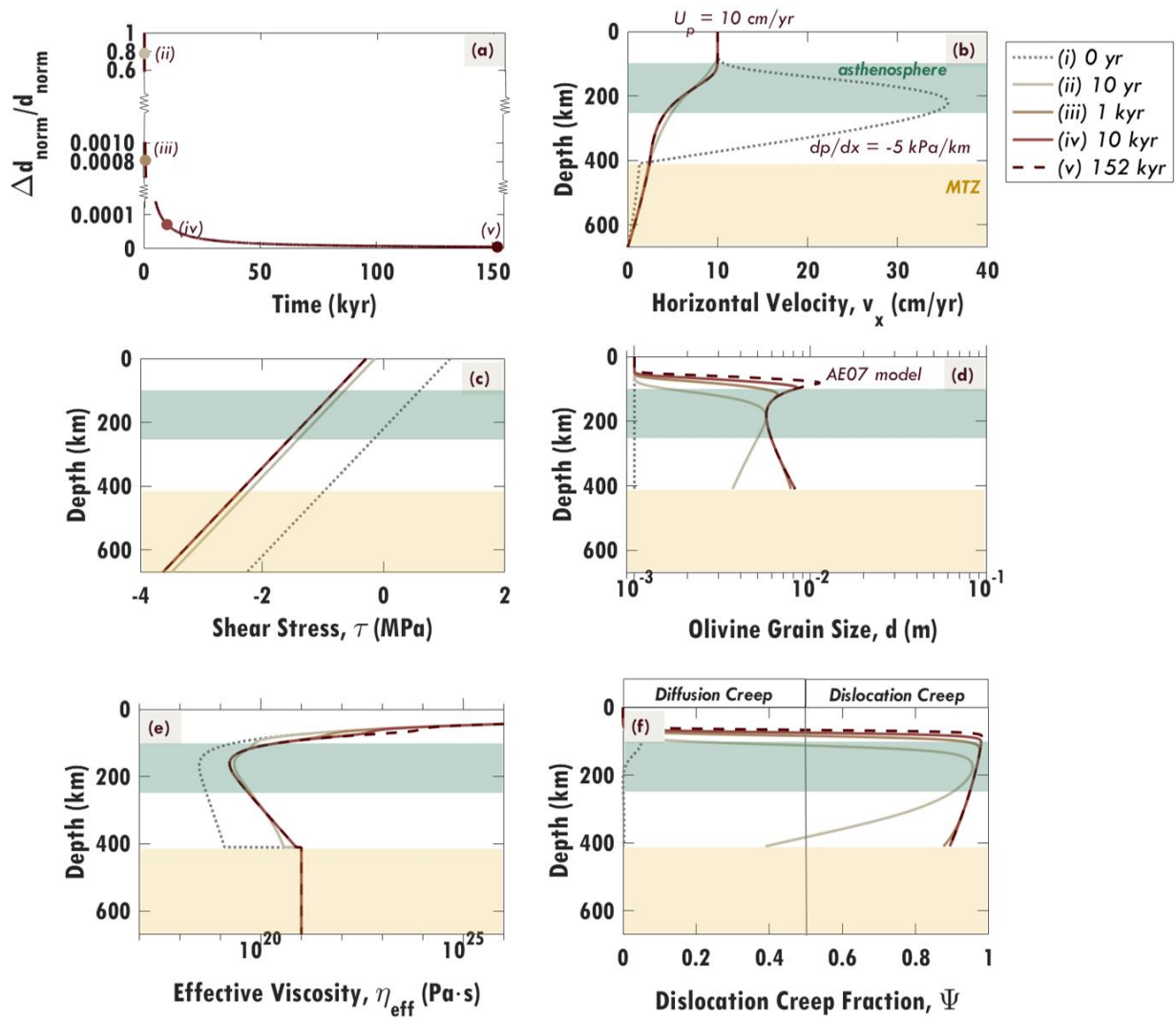


Figure 3. Temporal evolution of flow with an imposed pressure gradient (-5 kPa/km) and plate velocity (10 cm/yr). The upper mantle (above 410 km) is dry (50 ppm H/Si) and has an initial (at 0 yr) constant (10^{-3} m or 1 mm) olivine grain-size. The mantle transition zone (MTZ, yellow region, 410-670 km) with a viscosity of 10^{21} Pa · s is assumed to deform together with the upper mantle. During the deformation induced by the flow (b), olivine grain-sizes evolve (d) following the AE07 model (Austin and Evans, 2007) as in Equation (7) until the grain-size structure stabilizes (in panel (a), which shows the time evolution of the convergence criterion ($\Delta d_{\text{norm}}/d_{\text{norm}}$ for timestep $\Delta t = 10$ yr; Supplementary Information D)) after 152 kyr. Consequently, the flow configuration (b), shear stress profiles (c), effective viscosity (e) and the deformation type (f) evolve and stabilize. The initially PFn1 flow (dotted line) becomes dominantly Couette flow because the increased grain-size (d) leads to a greater upper mantle viscosity (e). The green region is the asthenosphere (100 -250 km), with a low viscosity zone (e).

181 time in the oceanic mantle (Figure 3). Here we consider a 10 cm/yr plate velocity and -5 kPa/km
 182 pressure gradient across the dry (50 ppm H/Si) upper mantle and a 10^{21} Pa·s mantle transition
 183 zone (MTZ). Initially (0 yr), we assume a constant grain-size of 1 mm that results in a *PFn1*

184 flow (Figure 3b) because this small grain size induces low effective viscosity (Figure 3e). Given
185 enough time, olivine grain-sizes evolve during the flow-driven deformation to a steady-state
186 structure (Figure 3a and 3d). We find that steady state is reached after only 152 kyr (only 0.3%
187 of the plate age), which is significantly quicker than mantle flow time scales. This indicates that
188 the grain size is always in effective equilibrium for steady-state mantle flow problems, and that
189 the adjustment associated with the grain-size evolution (Figure 3d) and the associated changes
190 to the flow field (Figure 3b), stresses (Figure 3c), viscosity (Figure 3e) and deformation style
191 (Figure 3f), can be considered essentially instantaneous.

192 Although the initial grain size does not affect the final grain size at steady state (Supplementary
193 Information E.1), the choice of initial grain size does affect the time it takes the grain size to
194 stabilize (Figure S3). A larger initial grain size (e.g., 10 mm) stabilizes faster than a smaller
195 grain size (1 mm), because large grains subdivide more rapidly than small grains, which tend
196 to grow before subdividing (Equation 7). In the following section, we assume an initial grain
197 size of 10 mm because it reaches steady state faster, and thus reduces calculation time.

198 **4. Link between flow configurations and rheologies of the oceanic upper mantle**

199 Here, we investigate how water content, grain-size, the imposed plate velocity and the
200 horizontal pressure gradient control the dominant flow configuration of the upper mantle
201 (Figure 4). We consider dry (50 ppm H/Si) and wet (1000 ppm H/Si) conditions for layers above
202 the mantle transition zone, and assign 10^{21} Pa·s for mantle transition zone viscosity if the upper
203 mantle is dry and 10^{20} Pa·s if it is wet. This setup maintains comparable effective viscosities
204 for the upper mantle and mantle transition zone layers, and we investigate flow configurations
205 for contrasting rheologies later (Section 7). We vary the plate velocity between 0 and 10 cm/yr
206 in the direction of pressure-driven flow, and horizontal pressure gradients between 0 and -5
207 kPa/km (e.g., Natarov and Conrad, 2012).

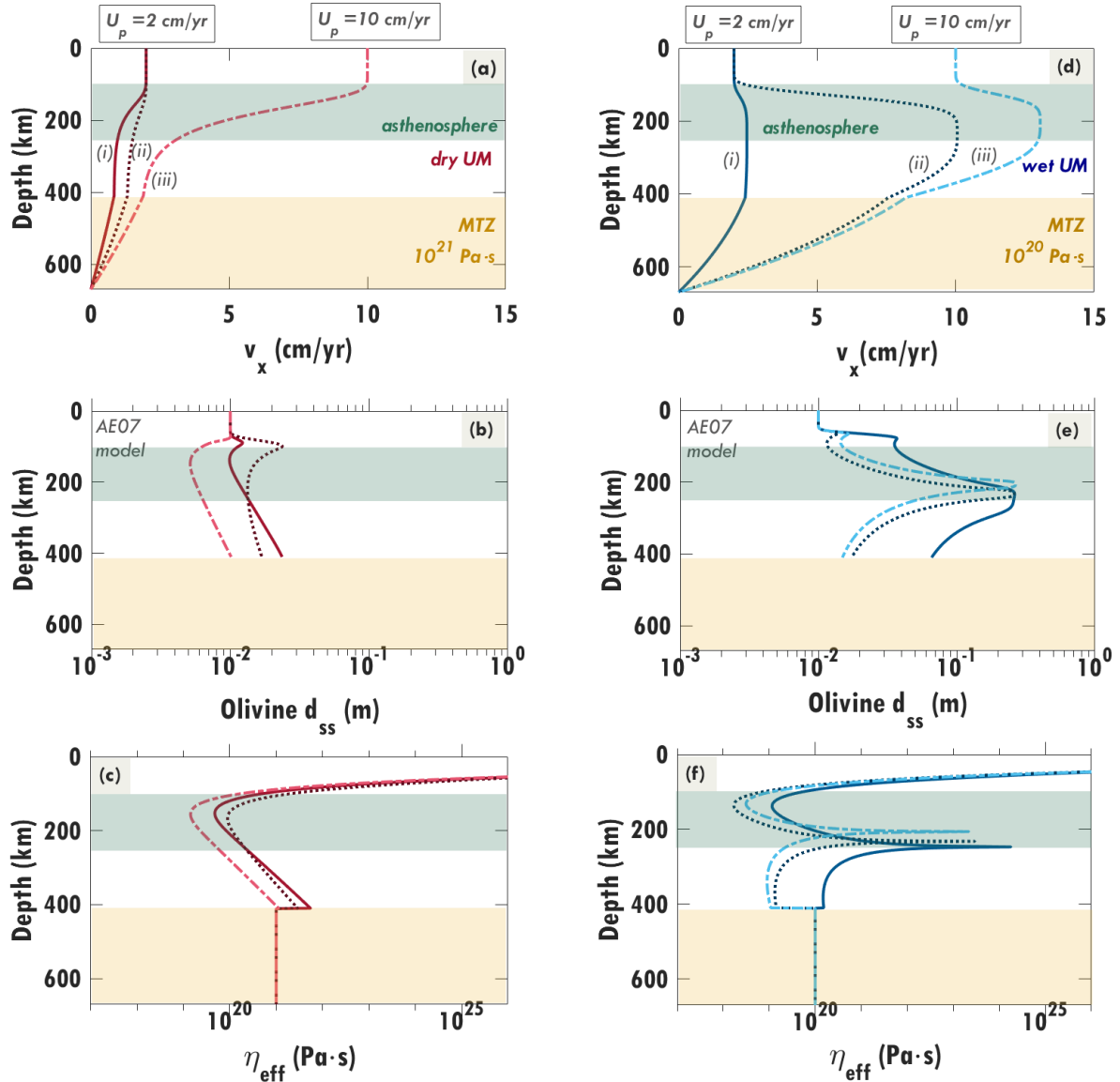


Figure 4. Factors affecting upper mantle flow (a, d), grain-size (b, e), and viscosity (c, f) at steady state for dry (a-c) and wet (d-f) conditions. Different combinations of imposed plate velocity and horizontal pressure gradient (labeled as i, ii and iii) are considered, where U_p and dp/dx are (i) 2 cm/yr and -1 kPa/km, (ii) 2 cm/yr and -3 kPa/km, and (iii) 10 cm/yr and -3 kPa/km. Dry upper mantle (50 ppm H/Si) flows via Couette flow (a) while wet upper mantle (1000 ppm H/Si) flows via PFn3 (d). Nonetheless, grain size reduction in the asthenosphere (b, e) results in a low viscosity zone (c, f). Grain growth at the bottom of the asthenosphere occurs only for PFn3 (e) because of very low flow-induced-stresses, and produces a peak in viscosity (f).

208 The water content of the upper mantle controls rheology both directly via weakening minerals
 209 and indirectly via grain-size evolution, and thus determines the type of flow. We find that if
 210 water is present in the upper mantle, *PFn3* is likely to dominate (Figure 4d). Otherwise, Couette
 211 flow dominates (Figure 4a) because the higher viscosities associated with a dry upper mantle
 212 do not permit Poiseuille flow. As a feedback mechanism, the flow configuration dictates the

213 grain-size structure and thus also the viscosity structure. If the upper mantle is *PFn3*-dominated
214 (Figure 4d), a viscosity peak (Figure 4f) develops, associated with very large grain-sizes (Figure
215 4e). Such large grain-sizes form in the mid-upper mantle because plug flow (*PFn3*) features
216 approximately constant horizontal velocities, and deformation is therefore minimal and grain-
217 size reduction is slow (Equation 7). Extensive shearing above and below the non-deforming
218 region results in significant grain-size and viscosity reduction in both the shallow and deep
219 upper mantle. In contrast, a Couette-flow-dominated upper mantle (Figure 4a), which is more
220 typical of dry conditions, features grain-sizes that gradually increase with depth (Figure 4b) and
221 is associated increasing effective viscosity (Figure 4c). Regardless of the flow configuration,
222 the grain-size reduction due to shear deformation controls the low viscosity zone in the
223 asthenosphere. In general, an increase in the magnitude of the horizontal pressure gradient
224 increases the stress induced by pressure-driven flow, which eventually overwhelms plate-driven
225 flow (case i vs. ii, Figure 4d). The resulting increase in stress produces smaller grain-sizes,
226 which may make diffusion creep important ($\Psi < 1$). However, in our forward models, the grain
227 sizes remain larger than ~ 3 mm (as in Figure 3d), which is large enough for dislocation creep
228 to remain dominant.

229 **5. Predicted seismic structures for dry and wet oceanic upper mantle**

230 To quantify the impact of flow configurations on upper mantle seismic structure, we estimate
231 the shear wave velocity V_s and seismic quality factor Q for the steady-state grain sizes associated
232 with the different plate velocity and pressure-gradient combinations considered in Section 4.
233 We estimate V_s (Figure 5b and 5d) following the formulation of Karato (1993), which is Q -
234 dependent. We calculate the Q factor (Figure 5a and 5c) using the grain-size dependent
235 formulation of Jackson and Faul (2010) at 100 s period, which is representative for seismic
236 imaging of the upper mantle (e.g., Debayle, et al., 2020).

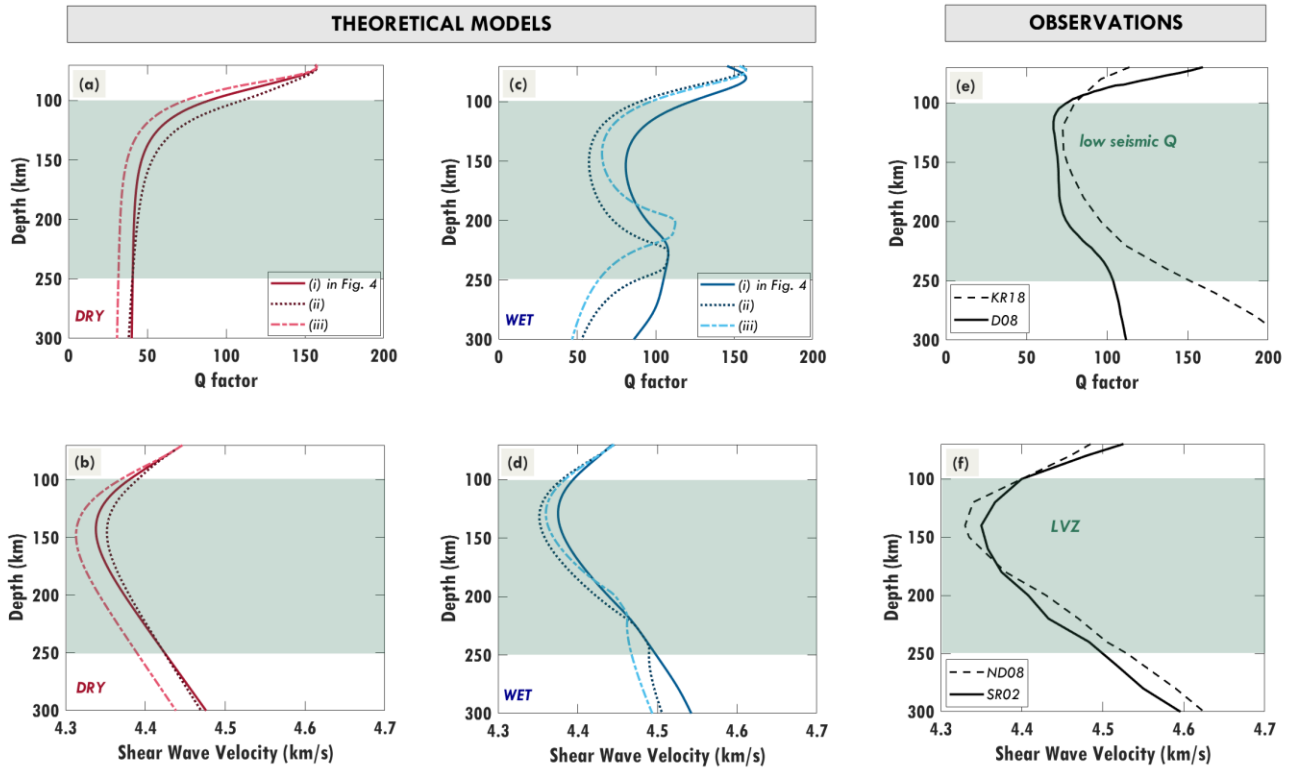


Figure 5. (a-d) Theoretical seismic models, computed for cases (i) to (iii) from Figure 4. The theoretical Q values for dry (a) and wet (c) conditions are calculated using the steady-state grain sizes in Figure 4b and 4e, as are the theoretical shear wave velocity profiles (b and d). **(e) Observations of Seismic Q** for comparison are the KR18 global Q model of Karaoglu and Romanowicz (2018) and the D08 model of Dalton et al. (2008) for mid-age oceans. **(f) Seismic velocity models** for comparison are the ND08 velocity model of Nettles and Dziewonski (2008) for 25-100 Myr old oceanic plate ages and SR02 model of Shapiro and Ritzwoller (2002) for 75 Myr age. The green region indicates the seismically anomalous asthenosphere (100-250 km depth) identified in Figure 1. All theoretical models except for Q within a dry upper mantle (panel (a)) show negative anomalies in the asthenosphere.

237 5.1 Effect of water content and flow configuration on seismic structures

238 Different grain size structures for dry (Figure 4b) and wet (Figure 4e) conditions result in
 239 different profiles for seismic Q (Figure 5a and 5c) and shear wave speeds (Figure 5b and 5d).
 240 Thus, water content indirectly, but significantly, impacts seismic signatures via flow-affected
 241 grain-size evolution. Notably, although we can produce the seismic shear wave trends of the
 242 LVZ regardless of the water content and flow configuration, this is not true of the low Q zone
 243 in the asthenosphere. For dry upper mantle flowing via Couette flow, the predicted seismic Q
 244 profile (Figure 5a) does not show a pronounced low Q zone in the asthenosphere. Instead, Q
 245 becomes approximately constant with depth and consistently < 50 despite an increase in grain-

246 size with depth (6 mm – 30 mm, Figure 4b). In contrast, a wet upper mantle deformed via $PFn3$
247 produces a zone of low seismic Q in the asthenosphere (Figure 5c). The magnitude and extent
248 of this zone are affected by the plate velocity and pressure gradient combination because of the
249 stress-dependent grain size evolution. Indeed, the grain-size structure produced by the $PFn3$
250 configuration affects both the Q structure and the V_s profile. For instance, the Q and V_s peaks
251 within the lower asthenosphere (200 – 250 km) are caused by the grain-size peak (Figure 4e)
252 associated with weak shearing in this region. However, this is not evident for Couette-
253 dominated dry asthenosphere because the grain size increase is much smaller (Figure 4b) than
254 it is for $PFn3$ -dominated wet asthenosphere (Figure 4e).

255 **5.2 Comparison between theoretical seismic models and observations**

256 In practice, reported Q models (Figure 5e) are globally-sourced profiles, which limits spatial
257 resolution and may cancel out some localized features. The shear wave velocity observations
258 presented here are averaged for oceanic plates of similar ages (i.e., mid-age plates, Figure 5f),
259 and thus should be comparable with our curves for an assumed 60 Myr old oceanic plate (Figure
260 5b and 5d). However, because of averaging across plates with different speeds and pressure
261 gradients, we are limited in our comparisons between predicted and observed Q and V_s , which
262 assume single choices of these parameters. Instead, we compare overall trends between the
263 theoretical and geophysical models, and later attempt to infer the dominant type of flow in the
264 oceanic upper mantle from the seismic observations (Figure 7, Section 7).

265 Although the $PFn3$ configuration produces a low Q zone that is comparable to the observations
266 (Section 5.1), the predicted Q below the asthenosphere does not continue to increase for all
267 cases (Figure 5c). Observations show $Q > 100$ below the asthenosphere (Figure 5e), which
268 requires grain-sizes larger than 10 cm (e.g., case i, Figure 4e). We may increase the grain size
269 significantly (> 10 cm) by introducing high water content below the asthenosphere (Section
270 5.3) and low stresses that favor grain growth in this region. This requires a $PFn3$ configuration

271 that spans the entire upper mantle and mantle transition zone (i.e., case i, Figure 4d) and that is
 272 not confined to the upper mantle above 410 km (as for cases ii and iii).

273 5.3 Impact of partial melt and water distribution on seismic structures

274 The shallow upper mantle or asthenosphere has been proposed to be water-undersaturated and
 275 to contain unextractable melt (e.g., Selway and O'Donnell, 2019; Debayle et al, 2020), while
 276 the deeper upper mantle may contain no melt and a higher water content (e.g., Selway et al.,
 277 2019; Selway and O'Donnell, 2019). Here we test how such conditions would affect upper
 278 mantle flow and associated seismic observations. We consider a -1 kPa/km pressure gradient
 279 and a plate speed of 2 cm/yr (as in case i) and assume an increasing water content with depth
 280 in the upper mantle (Figure 6a.1). We compute the associated flow configuration (Figure S6a,
 281 Supplementray Information E.4), which is $PFn3$ across the uppermost 670 km of the mantle,
 282 and the associated grain-size structure (Figure S6b). The predicted Q profile (pink line, Figure
 283 6b) lies close to the observations and overlaps well with the Dalton et al. (2008) (D08) model

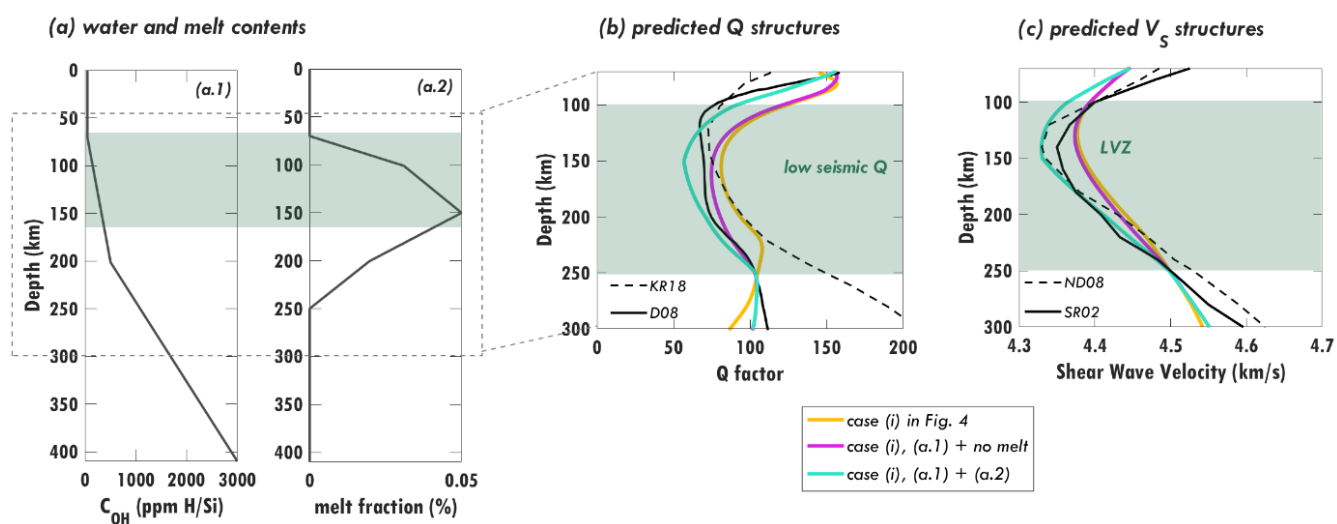


Figure 6. Impact of water content (a.1) and partial melt distribution (a.2) on predicted seismic structures (b-c). The melt fraction in the asthenosphere is calculated as $x - 0.10\%$ where x (in %) is estimated from Debayle et al. (2020) models for a plate moving with a speed of 2 cm/yr. The Jackson and Faul (2010) formulation for Q is used to predict the seismic structures for a melt-free upper mantle using the flow-induced grain sizes, and the Chantel et al. (2016) formulation is used in addition to Jackson and Faul (2010) when melt is present. The seismic observations in (b) and (c) are the same as in Figure 5e and f, respectively.

284 for mid-age plates in the lower asthenosphere. Below the asthenosphere, the predicted Q is
285 larger than that of the constant-water (1000 ppm H/Si) assumption (yellow line, Figure 6b) and
286 closer to observations. In contrast to the Q responses, the predicted V_s profiles for models with
287 different water contents (yellow and pink lines, Figure 6c) mostly overlap and have larger
288 minimum V_s in the LVZ than the observations.

289 We examine the effect of melt by introducing a melt distribution scenario (Figure 6a.2, $x =$
290 0.10%) where x in % is estimated from Debayle et al. (2020) models for a plate moving with
291 a speed of 2 cm/yr. We constrain the melt fraction to $< 0.3\%$, which is the suggested melt
292 fraction for the asthenosphere (e.g., Selway and O'Donnell, 2019; Debayle et al., 2020). This
293 small amount of melt reduces the viscosity of the asthenosphere only slightly, by a factor greater
294 than ~ 0.8 , when using olivine flow laws (Equations 4 and 5.1 to 5.4), which has a negligible
295 effect on upper mantle flow, grain-sizes, and rheology (Figure S6, Supplementary Information
296 E.4). However, the additional melt does significantly affect seismic Q and V_s (Chantel et al.,
297 2016). Adding melt into the asthenosphere of mostly wet upper mantle produces seismic V_s
298 structures that follow the observations more closely than those of melt-free assumptions (light
299 green line, Figure 6c). Overall, adding melt to the asthenosphere (which decreases both Q and
300 V_s) and introducing high water content to the deep upper mantle (which increases grain size and
301 Q) improves the fit to observations for our predicted seismic structures. Notably, a fast-moving
302 plate (case iii, Figure 4d), which produces larger grain sizes in the asthenosphere (Figure 4e)
303 than a slow plate (case ii), may require even more melt (Debayle et al., 2020) to reduce the
304 seismic Q further.

305 **6. Discussion**

306 In this 1-D analytical study, we assume a composite rheology (dislocation and diffusion creep
307 mechanisms) for olivine to represent the bulk rheology above 410 km since olivine is the most

308 abundant and well-studied mineral. The inherent viscosity of other phases such as pyroxenes
309 (e.g., Chen et al., 2006) and the effect of multiple phases on the overall rheology may
310 additionally affect the predicted type of flow. We assume that the mantle transition zone has
311 constant viscosity and flows under diffusion creep (*PFn1*-dominated). If the mantle transition
312 zone is assumed to flow under dislocation creep with wet upper mantle above it (entirely *PFn3*-
313 dominated above 670 km), this may increase the predicted Q below the asthenosphere where
314 grain-sizes may increase due to low stresses induced by the *PFn3* configuration.

315 Empirically, seismic Q increases with increasing grain size (e.g., Jackson and Faul, 2010) but
316 neither the magnitude nor the seismic period range of the minimum Q in the asthenosphere are
317 well constrained by experiments. There may be other factors influencing attenuation that we do
318 not account for in the estimation, such as oxygen fugacity that may decrease below the
319 asthenosphere and can cause an increase in Q (e.g., Cline et al., 2018). In addition, we consider
320 a single geological setting that is not perfectly comparable with the spherically averaged seismic
321 Q models and velocity models, which may cancel out heterogeneities. Averaging our predicted
322 seismic profiles across a range of imposed plate velocities and pressure gradients may improve
323 the usefulness of our theoretical seismic models when compared to globally-averaged
324 observations.

325 Since water distribution indirectly affects the prediction of seismic structures, accounting for
326 inferred water contents from magnetotelluric (MT) surveys in the oceanic upper mantle (e.g.,
327 Selway et al., 2019) may improve our forward models. Although the small amount of melt
328 fraction considered in this study, which is also detectable by MT surveys, has a negligible effect
329 on the viscosity and flow configuration (Figure S6) when using olivine flow laws, it can
330 potentially affect asthenospheric deformation if the melt is aligned (e.g., Wang et al. 2013;
331 Hansen et al., 2021), and may have a significant impact on diffusion creep viscosity if the melt
332 is well-connected (e.g., Holtzman, 2016).

333 The depth of base of the asthenosphere and the velocity boundary conditions there are not well
334 constrained. This is why we extend our 1-D model to 670 km, which should reduce any
335 boundary effects. However, we have found that the rheology contrast between the mantle
336 transition zone and the overlying upper mantle significantly affects the distribution of flow
337 between these layers (Figure S5) and is poorly constrained. Furthermore, the rheology of the
338 mantle transition zone, and the mantle above it, may vary laterally because of lateral variations
339 in hydration of the transition zone (e.g., Karlsen et al., 2019).

340 Since we consider 1-D mantle flow, we assume that pressure-driven flow and the surface plate
341 move in the same direction. However, a possible transverse component of the horizontal
342 pressure gradient relative to the plate motion (essentially a 2D problem) will affect the
343 interaction between the two flows, particularly for non-Newtonian rheology (Natarov and
344 Conrad, 2012), and thus also the predicted variations in grain size, seismic velocity, attenuation
345 and anisotropy. Investigating such 2D variations is beyond the scope of this study.

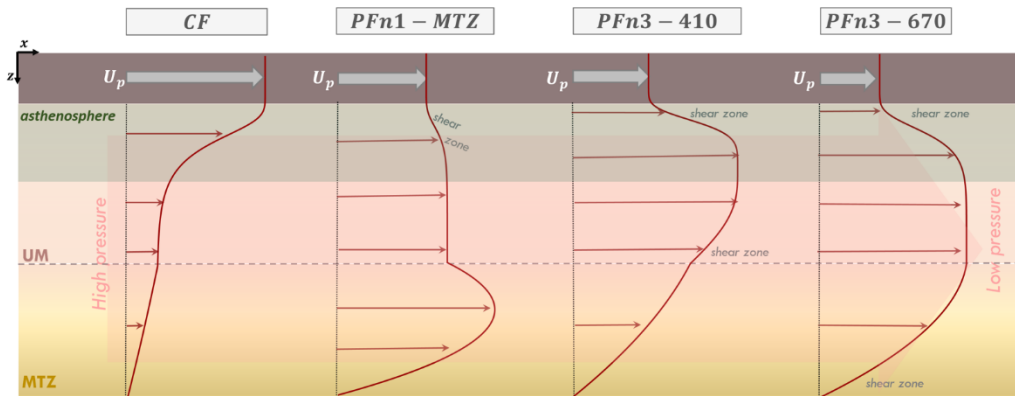
346 7. Flow configurations for the upper mantle

347 Our models suggest four possible flow configurations (Figure 7a) above 670 km depth,
348 depending on the drivers of the flow and the viscosity contrast between upper mantle and mantle
349 transition zone:

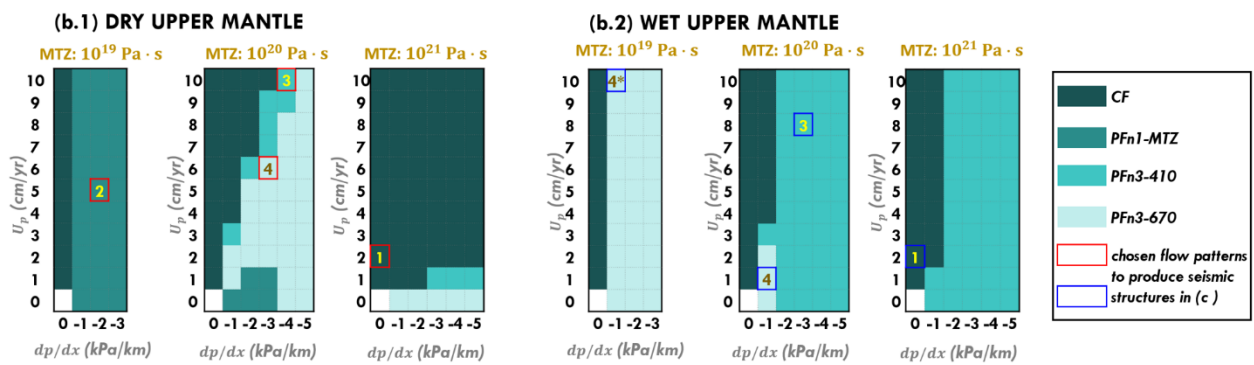
350 [1] *CF*: Couette flow dominates across the uppermost 670 km if the upper mantle and mantle
351 transition zone are both strongly viscous (e.g., if they are dry). This occurs if pressure gradients
352 in the channel are not large enough to drive flow within the highly viscous channel.

353 [2] *PFnI-MTZ*: Poiseuille flow dominates in the MTZ with little deformation in the upper
354 mantle if the mantle transition zone is significantly less viscous than the upper mantle. This is
355 because higher viscosities in the upper mantle prevent deformation, which instead becomes

(a) Flow configurations in the uppermost 670 km



(b) Different conditions to produce the different flow patterns



(c) Seismic structures produced by the different flow patterns

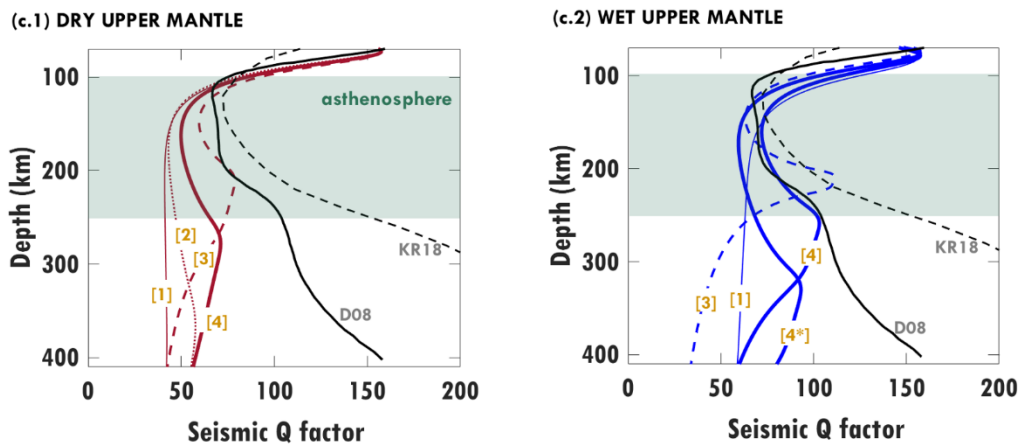


Figure 7. (a) A schematic diagram for different flow configurations that may dominate in the oceanic upper mantle and MTZ. (b) The dominant flow for different plate velocity (U_p) and horizontal pressure gradient (dp/dx) combinations for (b.1) dry (50 ppm H/Si) and (b.2) wet (1000 ppm H/Si) conditions, for different MTZ viscosities. (c) Predictions of seismic Q factor for different flow configurations for (c.1) dry and (c.2) wet conditions, where the type of flow configuration from (a) is indicated by a label [1]-[4] from (a) that also refers to the (U_p , dp/dx) combination used to drive the flow, as indicated in (b.1) and (b.2) above. Note that flow configuration [2] does not occur for wet conditions. Observations of seismic Q for comparison are the KR18 global Q model of Karaoglu and Romanowicz (2018) and the D08 model of Dalton et al. (2008) for mid-age oceans. Abbreviations: UM = upper mantle, MTZ = mantle transition zone, CF = Couette flow, and PF = Poesuille flow (PFn1 for Newtonian PF and PFn3 for plug flow, see Figure 2a and 2b).

357 (thus *PFn1*-dominated).

358 **[3] *PFn3-410***: Plug flow occurs dominantly in the upper mantle if the mantle transition zone
359 is more viscous than the upper mantle. Here deformation concentrates within the less viscous
360 (typically wet) upper mantle, and the pressure gradient must be large enough that plug flow
361 exceeds the plate-driven Couette flow.

362 **[4] *PFn3-670***: Plug flow may dominate across the uppermost 670 km if both the upper mantle
363 and mantle transition zone have sufficiently low viscosities (e.g., if they are wet) to allow
364 existing pressure gradients to drive flow or if pressure gradients are large enough to drive plug
365 flow in a viscous (dry) upper mantle.

366 Because of its impact on viscosity, water content helps to determine the dominant flow
367 configuration (Figure 7b). A dry upper mantle (Figure 7b.1) may exhibit any of these four flow
368 configurations, depending on the viscosity of mantle transition zone. A low-viscosity mantle
369 transition zone (10^{19} Pa·s) exhibits dominantly *PFn1-MTZ*, an intermediate viscosity (10^{20}
370 Pa·s) may produce any of the four configurations depending on flow drivers, and a highly
371 viscous mantle transition zone (10^{21} Pa·s) is stiff enough to only produce the *CF* configuration.
372 A wet upper mantle (Figure 7b.2) produces dominantly *PFn3* flow, either above 410 km if the
373 mantle transition zone is stiff enough to prevent deformation or above 670 km otherwise.

374 Seismic Q and velocity profiles can potentially constrain mantle flow. However, most of the
375 seismic structures reported are averaged globally or over a range of plate ages, which may
376 cancel out some localized features such as the peak seismic velocity and the peak seismic Q
377 within the asthenosphere, as predicted for *PFn3-410* (dashed lines labelled with [3], Figure 7c).
378 This limits our ability to compare forward seismic velocity and attenuation models with most
379 of the seismological observations, unless the observations are localized. Nonetheless, from our
380 forward models, a dominant *PFn3-670* configuration in the oceanic mantle above 670 km (solid

381 lines labelled with [4], Figure 7c) best explains the seismic Q minimum within the
382 asthenosphere. For this flow configuration, magnitudes of Q for wet upper mantle (Figure 7c.2)
383 are closer to the observations than those for dry upper mantle (Figure 7c.1) because the induced
384 dry olivine grain-sizes are too small (< 3 cm, Figure S7c) to explain the Q observations,
385 particularly beneath the asthenosphere.

386 8. Conclusions

387 As a summary, we propose the following to explain the observed seismic structures, particularly
388 the observed low-Q zone:

- 389 (i) Poiseuille flow (*PF*), and particularly plug flow (*PFn3*), may dominate deformation
390 within the oceanic upper mantle. Wet conditions facilitate this type of flow because
391 they reduce upper mantle viscosity, allowing ambient mantle pressure gradients to
392 drive plug flow that can overprint plate-driven shearing (Couette flow, *CF*).
- 393 (ii) Variations in grain size induced by plug flow (*PFn3*) are necessary to explain the
394 zone of low Q (high seismic attenuation) in the asthenosphere. Here, low Q can be
395 attributed to grain-size reduction due to extensive shearing within the low viscosity
396 asthenosphere.
- 397 (iii) The increase of Q beneath the asthenosphere can be explained by large grain-sizes
398 associated with minimal deformation within the ~250-410 km depth range. Such
399 slow deformation is consistent with plug flow spanning the entire upper mantle and
400 transition zone (the *PFn3-670* flow configuration, Figure 7a).
- 401 (iv) High water content may be required to promote large grain sizes (> 10 cm) in the
402 mantle rocks beneath the asthenosphere.
- 403 (v) Melt in the asthenosphere is not necessary (e.g., Lin et al., 2016) to explain observed
404 seismic anomalies there. Instead, grain-size variations associated with plug flow

405 ($PFn3$) can explain both the low-Q and low velocity zones (LVZ). Small amounts
406 of melt can, however, amplify these trends, which can improve the fit to global
407 seismic observations (e.g., Figure 6).

408 Pressure-driven flow travelling beneath the oceanic lithosphere is important because it
409 promotes long-wavelength mantle convection (Semple and Lenardic, 2018), drives tectonic
410 plate motions (Semple and Lenardic, 2020), transports geochemical heterogeneities
411 (Yamamoto et al., 2007), and generates intraplate volcanism (Ballmer et al., 2013). Here we
412 have shown that pressure-driven plug flow may additionally explain pervasive seismic
413 observations such as the LVZ and the low-Q zone, by reducing asthenospheric grain-sizes.
414 Because this grain-size reduction also weakens asthenospheric rocks, plug flow helps to
415 maintain a low-viscosity asthenosphere, a key feature of Earth's interior structure that regulates
416 a variety of geodynamic process ranging from plate tectonics to postseismic and postglacial
417 relaxation (e.g., Richards and Lenardic, 2018).

418 **Acknowledgments**

419 This work was supported partly by the Research Council of Norway's projects 223272 (Centre
420 of Excellence) and 288449 (MAGPIE Project), and partly by the Australian Research Council
421 grant FT150100541.

422 **References**

- 423 Austin, N.J., and Evans, B. (2007). Paleowattmeters: A scaling relation for dynamically recrystallized
424 grain size. *Geology*, 35, 343-346. doi:10.1130/G23244A.1
- 425 Ballmer, M. D., Conrad, C. P., Smith, E. I. and Harmon, N. (2013). Non-hotspot volcano chains
426 produced by migration of shear-driven upwelling toward the East Pacific Rise. *Geology*, 41,
427 479-482, doi:10.1130/g33804.1.
- 428 Becker, T. (2006). On the effect of temperature and strain-rate dependent viscosity on global mantle
429 flow, net rotation, and plate-driving forces. *Geophys. J. Int.*, 167, 943-957. doi:
430 10.1111/j.1365-246X.2006.03172.x
- 431 Behn, M., Hirth, G. and Elsenbeck II, J. R. (2009). Implications of grain size evolution on the seismic
432 structure of the oceanic upper mantle. *Earth and Planetary Science Letters*, 282, 178-189. doi:
433 10.1016/j.epsl.2009.03.014
- 434 Chantel, J., Manthilake, G., Andrault, D., Novella, D., Yu, T., and Wang, Y. (2016). Experimental
435 evidence supports mantle partial melting in the asthenosphere. *Science Advances*, 2,
436 e1600246. doi:10.1126/sciadv.1600246
- 437 Cline II, C., Faul, U., David, E., Berry, A., and Jackson, I. (2018). Redox-influenced seismic
438 properties of upper-mantle olivine. *Nature*, 555, 355-358. doi:10.1038/nature25764
- 439 Dalton, C., Ekström, G., and Dziewonski, A. (2008). The global attenuation structure of the upper
440 mantle. *J. Geophys. Res.* 113, B09303. doi:10.1029/2007JB005429
- 441 Dalton, C., Ekström, G., and Dziewonski, A. (2009). Global seismological shear velocity and
442 attenuation: A comparison with experimental observations. *Earth and Planetary Science*
443 *Letters* 284, 65-75. doi:10.1016/j.epsl.2009.04.009
- 444 Debayle, E., Bodin, T., Durand, S. and Ricard, Y. (2020). Seismic evidence for partial melt below
445 tectonic plates. *Nature*, 586, 555-559. doi:10.1038/s41586-020-2809-4

- 446 Faul, U. and Jackson, I. (2005). The seismological signature of temperature and grain size variations in
447 the upper mantle. *Earth and Planetary Science Letters*, 234, 119-134.
448 doi:10.1016/j.epsl.2005.02.008
- 449 Forte, A., and Mitrovica, J. (1996). New inferences of mantle viscosity from joint inversion of long-
450 wavelength mantle convection and post-glacial rebound data. *Geophys. Res. Lett.* 23, 1147-
451 1150. doi:10.1029/96GL00964
- 452 Gutenberg (1959), *Physics of the Earth's Interior*, Springer, New York.
- 453 Hall, C. and Parmentier, E.M. (2003). Influence of grain size evolution on convective instability.
454 *Geochem. Geophys. Geosyst.*, 4, 1029. doi:10.1029/2002GC000308
- 455 Hansen, L., Faccenda, M., and Warren, J. (2021). A review of mechanisms generating seismic
456 anisotropy in the upper mantle. *Physics of the Earth and Planetary Interiors* 313, 106662. doi:
457 10.1016/j.pepi.2021.106662
- 458 Hirth, G., and Kohlstedt, D. (2003). Rheology of the Upper Mantle and the Mantle Wedge: A View
459 from the Experimentalists. *Inside the Subduction Factory, Geophysical Monograph*, 138, 83-
460 105.
- 461 Höink, T., and Lenardic, A. (2010). Long wavelength convection, Poiseuille–Couette flow in the low-
462 viscosity asthenosphere and the strength of plate margins. *Geophys. J. Int.* 180, 23–33. doi:
463 10.1111/j.1365-246X.2009.04404.x.
- 464 Holtzman, B. (2016). Questions on the existence, persistence, and mechanical effects of a very small
465 melt fraction in the asthenosphere. *Geochem. Geophys. Geosyst.*, 17, 470-484.
466 https://doi:10.1002/2015GC006102.
- 467 Jackson, I., and Faul, U. (2010). Grainsize-sensitive viscoelastic relaxation in olivine: Towards a
468 robust laboratory-based model for seismological application. *Physics of the Earth and*
469 *Planetary Interiors*, 183, 151-163. doi:10.1016/j.pepi.2010.09.005

- 470 Jung, H. and Karato, S. (2001). Water-induced fabric transitions in olivine, *Science*, 293, 1460-1463.
471 doi:10.1126/science.1062235
- 472 Karaoglu, H. and Romanowicz, B. (2018). Inferring global upper-mantle shear attenuation structure by
473 waveform tomography using spectral element method. *Geophys. J. Int.*, 213, 1536-1558. doi:
474 10.1093/gji/ggy030
- 475 Karato, S.-i. (1993). Importance of anelasticity in the interpretation of seismic tomography. *Geophys.*
476 *Res. Lett.*, 20, 1623-1626. <https://doi.org/10.1029/93GL01767>
- 477 Karato, S.-i. (2012). On the origin of the asthenosphere, *Earth and Planetary Science Letters* 321-322,
478 95-103. doi:10.1016/j.epsl.2012.01.001
- 479 Karato, S.-i., and Jung, H. (1998), Water, partial melting and origin of the seismic low velocity and
480 high attenuation zone in the upper mantle, *Earth and Planetary Science Letters* 157, 193-207.
- 481 Karlsen, K., Conrad, C. and Magni, V. (2019). Deep water cycling and sea level change since the
482 breakup of Pangea. *Geochemistry, Geophysics, Geosystems*, 20, 2919–2935. doi:
483 10.1029/2019GC008232
- 484 Kaufmann, G. and Lambeck, K. (2000). Mantle dynamics, postglacial rebound and the radial viscosity
485 profile. *Physics of the Earth and Planetary Interiors* 121, 301-324. doi:10.1016/s0031-
486 9201(00)00174-6
- 487 Lin, P.Y.P., Gaherty, J.B., Jin, G., Collins, J.A., Lizarralde, D., Evans, R.L., and Hirth, G. (2016).
488 High-resolution seismic constraints on flow dynamics in the oceanic asthenosphere. *Nature*
489 535, 538–541. doi: 10.1038/nature18012
- 490 Mei, S., and Kohlstedt, D. L. (2000). Influence of water on plastic deformation of olivine aggregates:
491 1. Diffusion creep regime. *Journal of Geophysical Research*, 105, 21457-21469. doi:
492 10.1029/2000jb900179

- 493 Natarov, S. and Conrad, C.P. (2012). The role of Poiseuille flow in creating depth-variation of
494 asthenospheric shear. *Geophys. J. Int.* 190, 1297-1310. doi: 10.1111/j.1365-
495 246X.2012.05562.x
- 496 Nettles, M. and Dziewonski, A. (2008). Radially anisotropic shear velocity structure of the upper
497 mantle globally and beneath North America. *Journal of Geophysical Research*, 113, B02303.
498 doi:10.1029/2006JB004819
- 499 Richards, M., Yang, W.-S., Baumgardner, J. and Bunge, H.-P. (2001). Role of a low-viscosity zone in
500 stabilizing plate tectonics: Implications for comparative terrestrial planetology. *Geochem.*
501 *Geophys. Geosyst.*, 2, 2000GC000115. doi:10.1029/2000GC000115
- 502 Richards, M. A., and A. Lenardic (2018). The Cathles Parameter (Ct): A Geodynamic Definition of
503 the Asthenosphere and Implications for the Nature of Plate Tectonics. *Geochemistry,*
504 *Geophysics, Geosystems*, 19(12), 4858-4875, doi:10.1029/2018GC007664.
- 505 Ritterbex, S., Carrez, P. and Cordier, P. (2020). Deformation across the mantle transition zone: A
506 theoretical mineral physics view. *Earth and Planetary Science Letters*, 547, 116438. doi:
507 10.1016/j.epsl.2020.116438
- 508 Selway, K., and O'Donnell, J. (2019). A small unextractable melt fraction as the cause for the low
509 velocity zone. *Earth and Planetary Science Letters*, 517, 117-124.
510 doi:10.1016/j.epsl.2019.04.012
- 511 Selway, J., O'Donnell, J.P., and Özaydin, S. (2019). Upper Mantle Melt Distribution From
512 Petrologically Constrained Magnetotellurics. *Geochem. Geophys. Geosys.* 20, 3328-3346. doi:
513 10.1029/2019GC008227
- 514 Semple, A. and Lenardic, A. (2018). Plug flow in the Earth's asthenosphere. *Earth and Planetary*
515 *Science Letters*, 496, 29-36. doi: 10.1016/j.epsl.2018.05.030

- 516 Semple, A., and Lenardic, A. (2020). The Robustness of Pressure-Driven Asthenospheric Flow in
517 Mantle Convection Models With Plate-Like Behavior, *Geophysical Research Letters*, 47(17),
518 e2020GL089556, doi:10.1029/2020gl089556.
- 519 Shapiro, N.M. and Ritzwoller, M.H. (2002). Monte-Carlo inversion for a global shear-velocity model
520 of the crust and upper mantle. *Geophys. J. Int.* 151, 88-105. doi:10.1046/j.1365-
521 246X.2002.01742.x
- 522 Steinberger, B. and Calderwood, A. (2006). Models of large-scale viscous flow in the Earth's mantle
523 with constraints from mineral physics and surface observations. *Geophys. J. Int.* 167, 1461-
524 1481. doi: 10.1111/j.1365-246X.2006.03131.x
- 525 Tommasi, A., Tikoff, B. and Vauchez, A. (1999). Upper mantle tectonics: three-dimensional
526 deformation, olivine crystallographic fabrics and seismic properties. *Earth and Planetary
527 Science Letters*, 168, 173-186. doi:10.1016/S0012-821X(99)00046-1
- 528 Turcotte, D., and Schubert, G. (2014). *Geodynamics* (3rd ed.). New York: Cambridge
529 University Press.
- 530 Wang, N., Montagner, J.P., Fichtner, A., and Capdeville, Y. (2013). Intrinsic versus extrinsic
531 seismic anisotropy: The radial anisotropy in reference Earth models. *Geophys. Res.
532 Lett.*, 40, 4284-4288. doi: 10.1002/grl.50873
- 533 Warren, J. and Hirth, G. (2006). Grain size sensitive deformation mechanisms in naturally deformed
534 peridotites. *Earth and Planetary Science Letters*, 248, 438-450.
535 doi:10.1016/j.epsl.2006.06.006
- 536 Yamamoto, M., Morgan, J. P., Morgan, W. J., Foulger, G. R. and Jurdy, D. M. (2007). Global plume-
537 fed asthenosphere flow—I: Motivation and model development, in *Plates, Plumes and
538 Planetary Processes*, edited, p. 0, Geological Society of America, doi:10.1130/2007.2430(09).